JMEPEG (2010) 19:672–684
DOI: 10.1007/s11665-009-9536-1

1059-9495/$19.00

Modeling of AA5083 Material-Microstructure Evolution During Butt Friction-Stir Welding

M. Grujicic, G. Arakere, H.V. Yalavarthy, T. He, C.-F. Yen, and B.A. Cheeseman

(Submitted July 3, 2009)

A concise yet a fairly comprehensive overview of the friction stir welding (FSW) process is provided. This is followed by a computational investigation in which FSW behavior of a prototypical solution-strengthened and strain-hardened aluminum alloy, AA5083-H131, is modeled using a fully coupled thermo-mechanical finite-element procedure developed in our prior study. Particular attention is given to proper modeling of the welding work-piece material behavior during the FSW process. Specifically, competition and interactions between plastic-deformation and dynamic-recrystallization processes are considered to properly account for the material-microstructure evolution in the weld nugget zone. The results showed that with proper modeling of the material behavior under high-temperature/severe-plastic-deformation conditions, significantly improved agreement can be attained between the computed and measured post-FSW residual-stress and material-strength distribution results.

Keywords AA5083, finite element analysis, friction stir welding, Johnson-Cook strength model

1. Introduction

Friction stir welding (FSW) is a solid-state metal-joining process (Ref 1-3). Within FSW, a (typically) cylindrical tool-pin (threaded at the bottom and terminated with a circular-plate shape shoulder, at the top) is driven between two firmly clamped plates (placed on a rigid backing support), Fig. 1(a). Owing to a high normal downward pressure applied to the shoulder and owing to frictional sliding and plastic deformation, substantial amount of heat is generated at the tool/work-piece interface and in the region underneath the tool shoulder. Thermally plasticized work-piece material is then extruded around the traveling tool and forged into a welding joint behind the tool.

Owing to its solid-state character and lower process temperatures, FSW possesses a number of advantages and few limitations in comparison to the conventional fusion welding processes. A detailed discussion of the key advantages and limitations of the FSW process can be found in an excellent recent review by Nandan et al. (Ref 4). Also, a detailed account of the role of FSW in joining difficult-to-weld alloys (e.g., aluminum-based alloys can be found in Ref 4).

M. Grujicic, G. Arakere, H.V. Yalavarthy, and **T. He**, Department of Mechanical Engineering, Clemson University, 241 Engineering Innovation Building, Clemson, SC 29634-0921; and **C.-F. Yen** and **B.A. Cheeseman**, Army Research Laboratory – Survivability Materials Branch, Aberdeen Proving Ground, MD 21005-5069. Contact e-mails: mica.grujicic@ces.clemson.edu and mica@ces.clemson.edu.

FSW normally produces an asymmetric joint due to the fact that material flow during welding is different at two sides of the butting surfaces. The side at which the tool rotation is in the same direction as its travel direction is normally referred to as the "*advancing side*" while the other side is referred to as the "*retreating side*".

Microstructural examination of the FSW joints revealed the presence of four distinct zones, Fig. 1(b): In a decreasing order of the distance from the initial position of the butting surfaces the four zones are: (a) the unaffected zone; (b) The heat-affected zone, HAZ; (c) The thermo-mechanically affected zone, TMAZ; and (d) The weld-nugget/stir zone. A detailed description of various microstructural changes observed in these zones can be found in our prior study (Ref 5), as well as in later sections of this article.

The main objective of this study is twofold: First, a fairly comprehensive overview is provided of the main aspects of the FSW process with special emphasis placed on addressing complex relations between process parameters, heat and mass transfer phenomena and various microstructure-evolution processes which control the weld quality and process efficiency. The second objective of this study is to apply our recently developed fully coupled thermo-mechanical finite-element methodology (Ref 5) to model FSW behavior of a prototypical solution-strengthened and strain-hardened Al-Mg alloy AA5083-H131. Since AA5083-H131 is a non-age-hardenable alloy, its microstructural evolution is relatively simple, and mainly is the result of plastic deformation and dynamic recrystallization. In sharp contrast, microstructural changes in age-hardened alloys is typically much more complex and involves additional processes such as precipitate coarsening/agglomeration, dissolution, and re-precipitation in addition to plastic deformation and dynamic recovery/recrystallization.

The organization of the article is as follows: In Sect 2, a brief overview is provided of the key aspects of the processing/microstructure/property interrelations associated with the FSW process. This overview includes both the main

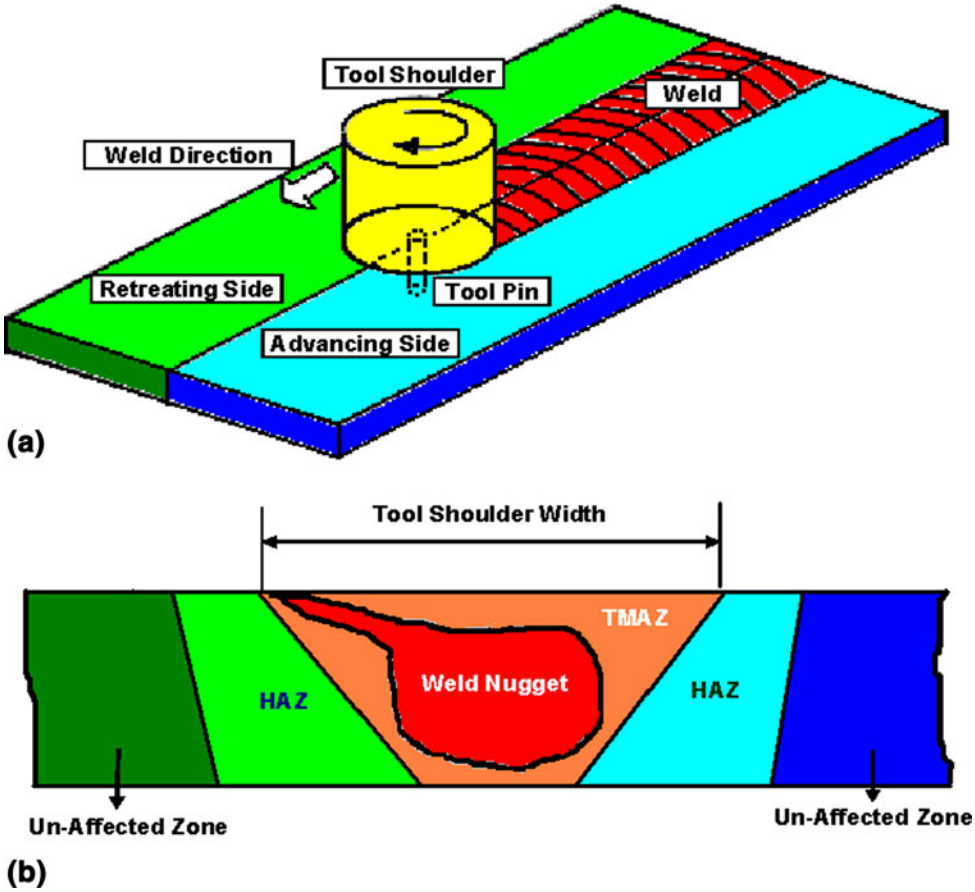

Fig. 1 (a) A schematic of the friction stir welding (FSW) process, and (b) the main microstructural zones associated with the typical FSW joint

experimental observations and the major FSW-process modeling efforts. The application of the fully coupled thermo-mechanical finite-element procedure developed in Ref 5 to modeling FSW behavior of AA5083-H131 is presented in Sect 3. A comparison between the computational and the experimental results pertaining to the post-FSW distributions of the residual stresses and material strengths is also provided in this section. The key conclusions resulting from this study are summarized in Sect 4.

2. Overview of the FSW Process

2.1 Heat Generation During the FSW Process

During FSW, heat is generated by the following processes (Ref 6-13): (a) frictional-sliding dissipation at the tool/work-piece contact surfaces; (b) plastic deformation of the work-piece material; and (to a lower extent) by (c) microstructural recovery and recrystallization. While plastic deformation also stores the energy in the form of dislocations, increased grain-boundary surface area, and increased surface area of sheared (cut-through or deformed) precipitates, this typically represents only a minor fraction (3-5%) of the total work of plastic deformation. The remainder is dissipated in the form of heat. In the remainder of this section, simple mathematical models are provided for the aforementioned components of heat generation.

Before deriving the appropriate equations for heat generation, one should define a relative velocity between the tool and the work-piece, v_r as follows:

$$v_r = \omega r - U \sin\theta \qquad \text{(Eq 1)}$$

where ω is the tool rotational speed, r a radial distance from the tool axis, U the tool travel speed, and θ an angle between the radial direction, r, and the welding direction.

The rate of heat generation due to frictional-sliding dissipation over an elementary contact surface area dA can be defined as (Ref 14):

$$d\dot{e}_f = \delta(\omega r - U \sin\theta)\mu_f p dA \qquad \text{(Eq 2)}$$

where δ is the extent of interfacial slip, μ_f the kinetic friction coefficient, and p the local tool/work-piece contact pressure. The conditions $\varepsilon = 1.0$ and $\varepsilon = 0.0$ correspond respectively to the cases when no sticking and complete sticking of the work-piece material to the tool takes place. In the first case, only frictional-slip dissipation contributes to the heat generation, while in the second case, heat is generated purely by plastic deformation/shearing of the work-piece material adhering to the tool.

When the work-piece material sticks to the tool and heat is generated by shearing of the work-piece material adjacent to the tool/work-piece interface, the heat generation rate can be defined as

$$d\dot{e}_s = (1-\delta)(\omega r - U \sin\theta)\tau_y dA \qquad \text{(Eq 3)}$$

where $\tau_y = \sigma_y/\sqrt{3}$ is the work-piece material shear strength while σ_y is the corresponding normal yield strength.

In addition to shearing of the work-piece material which adheres to the tool, plastic deformation of the work-piece material away from the tool/work-piece interface also generates heat. When the heat-plasticized work-piece material is modeled as a non-Newtonian fluid, the rate of heat generation, over a volume element dv, can be expressed as

$$d\dot{\varepsilon}_p = \beta\mu\phi dv \quad \text{(Eq 4)}$$

where β is the fraction of work of plastic deformation dissipated in the form of heat, μ the non-Newtonian viscosity of the plasticized work-piece material, while ϕ is defined as

$$\phi = 2\sum_{i=1}^{3}\left(\frac{\partial u_i}{\partial x_i}\right)^2 + \left(\frac{\partial u_1}{\partial x_2}+\frac{\partial u_2}{\partial x_1}\right)^2 + \left(\frac{\partial u_1}{\partial x_3}+\frac{\partial u_i}{\partial x_1}\right)^2 + \left(\frac{\partial u_3}{\partial x_2}+\frac{\partial u_2}{\partial x_3}\right)^2 \quad \text{(Eq 5)}$$

where u_i and x_i (i = 1, 2, 3) are the components of the material velocity and spatial coordinates.

When the work-piece material is treated as an elastic/plastic solid material, the rate of heat generation by dissipation of the plastic-deformation work is defined as

$$d\dot{e}_s = \beta\sigma_{ij}\dot{\varepsilon}_{p.ij}dv \quad \text{(Eq 6)}$$

where σ_{ij} and $\dot{\varepsilon}_{p.ij}$ represent stress and plastic strain-rate components and summation is implied over the repeated indices.

The mathematical models for heat generation presented above have been validated experimentally by either directly measuring thermal history of selected work-piece material points or, indirectly, by measuring mechanical energy expended during the FSW process (e.g., Ref 15).

2.2 Heat and Mass Transfer During the FSW Process

Except for the initial (*tool-insertion)* and the final (*tool-extraction*) stages of the FSW process, heat generation and heat/mass transfer can be assumed to occur under steady-state conditions (with respect to a coordinate frame attached to the traveling tool). Under this assumption, the velocity and temperature spatial distributions can be determined computationally by solving the appropriate steady-state mass, momentum, and energy conservation equations for and incompressible single-phase material.

2.2.1 Energy Conservation Equation. The steady-state energy conservation equation can be defined as

$$\rho C_p = \frac{\partial(u_i T)}{\partial x_i} = -\rho C_p U\frac{\partial T}{\partial x_1} + \frac{\partial}{\partial x_i}\left(k\frac{\partial T}{\partial x_i}\right) + S_b \quad \text{(Eq 7)}$$

where ρ is the work-piece material density, C_p the constant-pressure specific heat, u_i (i = 1, 2, 3) the material velocity components, T the temperature, k the thermal conductivity, while $S_b = d\dot{\varepsilon}_p/dv = \beta\mu\phi$ is the rate of heat generation per unit volume due to plastic-deformation work dissipation (away from the tool/work-piece interfaces).

The heat generated at the tool/work-piece interfaces due to frictional sliding and adhering-material shearing is partitioned between the work-piece and the tool in accordance with their thermo-physical properties as (Ref 16)

$$f = \frac{J_W}{J_T} = \frac{(k\rho C_p)_W^{1/2}}{(k\rho C_p)_T^{1/2}} \quad \text{(Eq 8)}$$

where subscripts W and T are used to denote the work-piece and the tool materials, respectively.

In order to complete the steady-state temperature-distribution problem definition, the temperature boundary conditions must be defined over the work-piece surfaces not in contact with the tool. Over the work-piece surface exposed to the ambient air, the equality between conduction heat-flux to the surface and a sum of the radiation and convection heat-fluxes from the work-piece surface is used as

$$k\frac{\partial T}{\partial z}_{top} = \sigma\varepsilon\left(T^4 - T_a^4\right) + h(T - T_a) \quad \text{(Eq 9)}$$

where σ ($= 5.67 \times 10^{-12}$ J K^{-4} cm^{-2} s^{-1}) is the Stefan-Boltzmann constant, ε the emissivity, T_a the ambient temperature, and h a heat-transfer coefficient.

In order to account for enhanced heat-transfer through the bottom of the work-piece (due to its contact with a metallic backing plate), an enhanced heat-convection type of boundary conditions is used as

$$k\frac{\partial T}{\partial z}_{bottom} = h_b(T - T_a) \quad \text{(Eq 10)}$$

where h_b is an "*enhanced*" heat transfer coefficient at the bottom surface of the work-piece.

2.2.2 Continuity Equation. When the work-piece material is modeled as an incompressible material, the mass conservation equation is defined as

$$\frac{\partial u_i}{\partial x_i} = 0 \quad \text{(Eq 11)}$$

2.2.3 Momentum Conservation Equation. With respect to the same coordinate system attached to the traveling tool, the momentum conservation equation is defined as

$$\rho\frac{\partial u_i u_j}{\partial x_i} = -\frac{\partial P}{\partial x_j} + \frac{\partial}{\partial x_i}\left(\mu\frac{\partial u_j}{\partial x_i} + \frac{\partial u_i}{\partial x_j}\right) - \rho U\frac{\partial u_j}{\partial x_1} \quad \text{(Eq 12)}$$

where ρ is a hydrodynamic pressure which drives the work-piece material flow.

The velocity boundary conditions at the tool/work-piece contact surfaces are defined as

$$u = (1-\delta)(\omega r\sin\theta - U); \quad v = (1-\delta)\omega r\cos\theta; \quad w = \varphi\omega \quad \text{(Eq 13)}$$

where u, v, and w are, respectively, the velocity components along the welding direction, an in-plane direction normal to the welding direction, and in the through-the thickness direction, φ is the pitch of the threaded cylindrical tool-pin, and the condition $w = 0$ holds at the work-piece/tool-shoulder interface.

2.2.4 Material Parameter Estimation. The utility of the mathematical modeling approach described above depends greatly on the accuracy and reliability of the values/functions used for various model parameters. Among these, the most critical ones are: non-Newtonian viscosity, μ,-enhanced heat transfer coefficient at the bottom surface of the work-piece, h_b, tool/work-piece static and kinetic friction coefficient, μ_f, and the extent of slip at the tool/work-piece interface. A detailed overview of the procedures, described below, used to assess and validate these parameters and their functional dependence on the FSW process parameters, and on the nature of the material(s) being welded can be found in the review article by Nandan et al. (Ref 4)

2.3 Work-Piece Material Flow and Joint Formation

Numerous experimental and computational investigations revealed that there are three main (simultaneously occurring components of the work-piece material motion during FSW (Ref 17-20):

(a) A layer of work-piece material in direct contact with the tool is forced to rotate around the tool by the tool/work-piece frictional forces;
(b) Threaded tool tends to push the material around it in the downward direction and, due to material-incompressibility condition, an upward motion of the work-piece material is also produced at a distance further away from the tool axis; and
(c) As the tool travels along the joining surfaces, the (thermally plasticized) work-piece material is forced to flow around the (rotating) tool.

In addition, it was clearly demonstrated that a majority of the material flow occurs through the retreating side and that the thermally plasticized material transported to the region behind the tool forms the welded joint.

Additional details regarding the material velocity field are obtained computationally (Ref 21, 22) and indirectly verified using inert markers embedded into the work-piece and determining their pre- and post-welding positions (e.g., Ref 23, 24), measuring the size and shape of the TMAZ (e.g., Ref 25), measuring the grain size which can be correlated with the local strain rates and, in terms, with local material velocities (e.g., Ref 26) or measuring the tool rotational torque and correlating it with the local shear strengths and deformation rates (e.g., Ref 27). These investigations jointly established the following picture regarding the material velocity field around the weld tool:

(a) There is a *rotational/recirculation* material zone around the tool whose width is larger at the top surface of the work-piece and the absolute value of this width depends on the work-piece material properties, the FSW process parameters, and the rate of heat transfer into the tool;
(b) Outside the re-circulated material zone the material transfer from the region in front of the tool to that behind the tool takes place mainly at the retreating side. In fact, at the advancing side often a flow-reversal/stagnant-zone is observed;
(c) At the top surface of the work-piece, the highest velocities are obtained in the regions underneath the tool shoulders. These are the overall highest material velocities. As the elevation through the work-piece decreases, the velocities decrease in magnitude, and the location of maximum velocities shifts toward the tool work-piece interface.

Among the other observed/predicted features of the material flow during FSW, the following ones appear unique and are worth mentioning:

(a) In contrast to conventional fusion welding techniques, in FSW material, mixing does not take place at the atomic level. Consequently, in the case of dissimilar-alloy FSW, striations of the two alloys (i.e., diffusion micro-couples) are often observed; and
(b) The character of the material velocity field and its interactions with material microstructure evolution (i.e., precipitate coarsening/agglomeration, grain and crystalline texture development, etc.) are believed to be the reason for the observation of the so-called "*onion-ring*" macro-structural features in the transverse cross-section of the FSW nugget region.

2.4 Temperature Fields and Post-Welding Cooling Rates

Since temperature fields and post-welding cooling rates can significantly affect the microstructure and properties of the different weld-joint regions, they require close examination. A review of the computational and (thermocouple-based and in situ neutron-diffraction-based) experimental studies dealing with this aspect of the FSW revealed the following unique features of the FSW temperature fields and cooling rates (e.g., Ref 4, 14, 28, 29):

(a) Owing to the fact that FSW is a solid-state joining process, peak temperatures are significantly lower than their counterparts encountered in fusion-based welding processes;
(b) Owing to a more diffuse nature of the heat source and lower welding rates, post-FSW cooling rates are generally lower;
(c) Temperature distribution in the transverse direction is generally non-symmetric with higher temperatures often located on the advancing side of the weld;
(d) Temperature distribution in the longitudinal direction is generally non-symmetric with substantially higher temperature gradients located in front of the traveling tool;
(e) Convective heat transfer by material flow plays an important role in the overall heat-transfer process, significantly affecting the temperature field and the post-welding cooling rates. If the thermally plasticized work-piece material in the weld zone is modeled as a fluid and heat transfer by the material flow treated as heat convection, then the corresponding Peclet number (a parameter which quantifies the relative importance of the heat transfer by convection to that by conduction) is typically of the order of few tens to a few hundreds. This finding confirms that material flow makes a major contribution to heat transfer in the FSW process (even in high thermal-conductivity materials); and
(f) Excessive temperatures and lower cooling rates may seriously alter both the precipitate and the grain microstructure and drastically change properties of the welded region relative to that of the base material(s).

2.5 FSW Process Parameters

The main FSW process parameters which control both the weld quality and ease of the welding process (i.e., process efficiency) are (a) tool rotational speed; (b) toll travel speed; (c) vertical pressure applied to the tool; (d) tool tilt angle; and (e) tool design. The heat-generation rate, the temperature field, the cooling rate, the tool-travel force, and the FSW torque/power all depend on these process parameters (Ref 28, 29).

Peak temperatures are generally found to increase with an increase in the tool rotational speed and contact pressure, and to decrease slightly with an increase in the welding speed.

Since welding torque is mainly controlled by the shear strength of the work-piece material (which decreases as

temperature increases), the same factors which lead to an increase in peak temperatures usually cause a reduction in the welding torque.

Weld quality depends, in a quite complex manner, on the FSW process parameters as well as on the nature of the material(s) being welded. In general, sufficient friction/plastic-deformation induced heating is required to promote material stirring/mixing while excessive heating must be avoided since it may lead to undesirable microstructure/property changes. Large welding torques are often an indication of insufficient heating which may not only lead to excessive tool wear or breakage, but also to inadequate material stirring/mixing which typically leads to microstructural defects.

2.6 The Effect of FSW-Tool Design

Tool design plays an important role in the FSW process affecting heat generation, material flow, weld quality as well as the power required for welding (Ref 30-33). While the tool shoulder is responsible for the majority of heat generation, both the tool shoulder and the tool pin affect material flow and the weld quality. Consequently, in recent years, various tool designs were proposed to improve the weld quality and efficiency of the FSW process. Many new FSW tool designs include taper threads and the flute which promote vertical motion of the material and more extensive heat generation (due to an increase in the tool-pin/work-piece contact area).

2.7 Formation of the FSW Flaws and Defects

When FSW is not carried out under appropriate processing conditions, various flaws/defects can form in the weld nugget and at its interface with the TMAZ region (Ref 34-37). Among the most often observed flaws are: (a) *worm-holes* (i.e., continuous channel-like voids localized on the advancing weld side near the nugget/TMAZ interface and extending in the welding direction) caused by inadequate material stirring (under an excessive tool travel-speed/rotational-speed ratio); (b) distributed void/micro-cracks located mainly at the weld-nugget/TMAZ interface which form as a result of large gradients in the material microstructure/properties, present in this region; (c) local "*soft spots*" associated with excessive-heating induced incipient melting (located mainly under the tool shoulder and near the pin/work-piece contact surfaces; and (d) pronounced flash tunnels (surface flaws) associated also with excessive heating (at the tool-shoulder/work-piece interface). Reducing the extent of flaws through proper selection of FSW process parameters is a major challenge in the FSW practice. In general, minimal defect contents are observed when large regions of the work-piece material are subjected to moderate to high strain rates (1-50 s^{-1}) and to temperatures 30-50 K below the solidus temperature and when (through the proper selection of tool design) more effective material stirring is attained (Ref 38).

2.8 Post-FSW Residual Stresses

Since FSW is associated with highly non-uniform distributions of plastic strain, temperature, and material microstructure, welded joints and the surrounding work-piece material typically contain significant post-welding residual stresses. Because the aforementioned non-uniformities are present in all the three principal directions, tri-dimensional residual stresses are often observed, although the through-the thickness component is often significantly lower in magnitude. Understanding the effect of FSW process parameters on the spatial distribution and the overall magnitude of the residual stresses is highly critical since residual stresses may lead to distortions and (tensile) residual stresses may promote crack initiation and propagation leading to catastrophic failure (Ref 21, 22, 39),

Numerous (x-ray/neutron diffraction and destructive hole-drilling based) experimental and (fluid-dynamics/solid-mechanics-based) computational investigations of the residual-stress distribution revealed the following general findings (Ref 40);

(a) Peak longitudinal stresses are generally higher than their transverse counterparts by roughly a factor of two;
(b) Tensile (longitudinal and transverse) residual stresses are normally found in the weld-nugget region while compressive stresses reside in the remainder of the weld/work-piece;
(c) While longitudinal stresses show a decent level of symmetry with respect to the initial position of the butting surfaces, the distribution of the transverse residual stresses is highly asymmetric. Specifically, on the retreating side, the transverse residual stresses mainly go to zero, while on the advancing side pronounced compressive transverse residual stresses are observed;
(d) The peak residual stresses (particularly their longitudinal components) increase significantly with an increase in the welding speed due to steeper temperature gradients present during FSW and reduced stress-relaxation times. On the other hand, no direct dependence of the residual stresses on the tool rotational speed is generally found; and
(e) The stirring action of the tool tends to relieve some of the stresses so often maximum residual stresses are found at the nugget-zone/TMAZ interface (Ref 41).

3. Computational Procedure

As mentioned earlier, modeling of the FSW process carried out in this study employed the fully coupled thermo-mechanical finite-element procedure developed in our prior study (Ref 5). Since a detailed account of the procedure was provided in Ref 5, only a brief overview of it will be presented in the remainder of this section.

3.1 Computational Domain

The computational domain used consists of a (40.0-mm radius, 3.0-mm thickness) circular plate (with a concentric through-the-thickness 3.0-mm radius circular hole) and a two-part tool (consisting of a 3.0-mm radius, 3.0-mm length solid right circular cylinder, at the bottom, and a 9.0-mm radius, 3.0-mm thickness circular-plate section, on the top), Fig. 2(a) and (b). The computational domain is meshed using ~20,000 first-order eight-node reduced-integration hexahedral thermo-mechanically coupled solid elements (the meshed model is not shown for brevity).

3.2 Computational Algorithm

The FSW process is analyzed computationally using a fully coupled thermo-mechanical finite-element algorithm within which heat dissipation associated with plastic deformation and

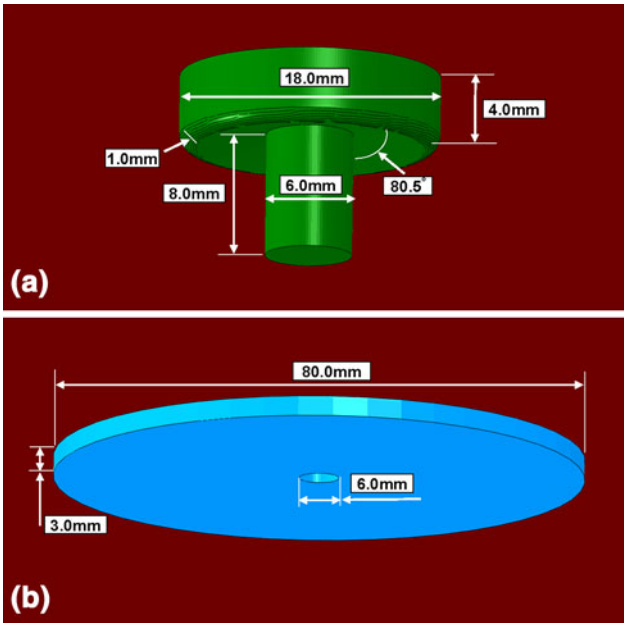

Fig. 2 Geometrical models with dimensions for the (a) FSW tool and (b) FSW work-piece

tool/work-piece interfacial friction-sliding is treated as a source in the governing thermal equations while the effect of temperature on the mechanical response of the work-piece material is taken into account through the use of a temperature-dependent work-piece material model.

The analysis is carried out by prescribing from the onset a constant rotational velocity and a constant downward pressure to the tool. Instead of assigning a travel velocity to the tool along the (postulated) butting surfaces of the work-piece, the work-piece material is forced to move through the work-piece computational domain at the same velocity, but in the opposite direction. Thus, Fig. 2(b) represents not the entire work-peace but rather a circular region around the tool in the otherwise infinitely long/wide work-piece. During the FSW process simulation, the material is prevented from flowing through the bottom face of the work-piece computational domain (to mimic the effect of rigid work-piece backing plate). Standard convective boundary conditions are applied over free surfaces of the work-piece and the tool, while enhanced convection boundary conditions are applied over the bottom face of the work-piece (to mimic the effect of enhanced heat extraction through the work-piece backing plate).

Work-piece/tool interactions are accounted for through the use of a penalty algorithm within which the extent of contact pressure is governed by the local surface penetrations while shear stresses are transferred via a "*slip/stick*" algorithm, that is, shear stresses lower than the frictional shear stress are transferred without interface sliding (otherwise interface sliding takes place). The frictional shear stress is defined by a modified Coulomb law within which there is an upper limit to the frictional shear stress (set equal to the shear strength of the work-piece material). The frictional shear stress is then defined as a smaller of the product between the static/kinetic friction coefficient and the contact pressure and the work-piece material shear strength.

As mentioned earlier, both plastic deformation and frictional sliding are treated as heat sources. In order to account for the fact that a small fraction of the plastic-deformation work is stored in the form of crystal defects, 95% of this work was assumed to be dissipated in the form of heat. As far as heat generation due to frictional sliding is concerned, it is assumed that its rate scale with the product of local interfacial shear stress and the sliding rate, and that 100% of this energy is dissipated in the form of heat. Partitioning of this heat between the tool and the work-piece is then computed using the appropriate thermal properties of the two materials.

As established earlier, the work-piece material in the nugget and TMAZ regions experience large plastic deformations during FSW under these circumstances: the use of a Lagrangian approach in which the finite-element mesh is attached to and moves with the material may display serious numerical problems (due to excessive mesh distortion). In order to overcome this approach, an Arbitrary Lagrangian Eulerian (ALE) formulation is used within which adaptive re-meshing is carried out to maintain good quality mesh.

The fully coupled thermo-mechanical problem dealing with FSW is solved using an explicit solution algorithm implemented in ABAQUS/Explicit (Ref 42), a general purpose finite element solver. In order to keep the computational cost reasonable while ensuring stability and robustness of the computational procedure, a mass scaling algorithm is used. This algorithm adaptively adjusts material density in the critical finite elements without significantly affecting accuracy of the computational results.

3.3 Material Models

Since the tool normally experiences relatively lower deformation during FSW, it is modeled using a rigid material. Its density and thermal properties are set to that of AISI-H13, the hot-worked tool steel which is often used as a FSW-tool material.

The work-piece material is assumed to be isotropic, linear-elastic, and strain-hardenable, strain-rate sensitive, thermally softenable plastic material and is modeled using the Johnson-Cook material model (Ref 43). Standard density and thermal properties for AA5083-H131 are used to define the thermal-portion of the material model.

While in the original Johnson-Cook material model temperature is assumed to affect the material strength through its effect on thermal activation of dislocation motion, exposure of the nugget-zone material to large plastic deformations and high temperature during FSW is generally found to result in dynamic recrystallization. Since this phenomenon is not accounted for in the original Johnson-Cook model, a modified version of this model will be proposed in next section. Essentially, in the modified Johnson-Cook model, strain hardening is still assumed to be related to the effective plastic strain, $\bar{\varepsilon}_{pl}$, via a parabolic relation, $B\bar{\varepsilon}_{pl}^{n}$, where B and n are the material parameters. However, $\bar{\varepsilon}_{pl}$ is taken to be composed of two terms: one (positive) associated with the operation of plastic deformation, and the other (negative) resulting from the operation of dynamic recrystallization.

4. Results and Discussion

4.1 Modification of the Johnson-Cook Material Strength Model

As mentioned earlier, the work-piece material AA5083-H131 is modeled using a modified Johnson-Cook

strain-hardening, strain-rate sensitive, temperature-softening yield-strength model. Within the original Johnson-Cook model, the yield strength is defined as (Ref 43):

$$\sigma_y = \left[A + B\left(\bar{\varepsilon}^{pl}\right)^n\right]\left[1 + C_1 \log\left(\dot{\bar{\varepsilon}}^{pl}/\dot{\bar{\varepsilon}}_0^{pl}\right)\right]\left[1 - T_H^m\right] \quad \text{(Eq 14)}$$

where $\bar{\varepsilon}^{pl}$ is the equivalent plastic strain, $\dot{\bar{\varepsilon}}^{pl}$ the equivalent plastic strain rate, $\dot{\bar{\varepsilon}}_0^{pl}$ a reference equivalent plastic strain rate, A the zero-plastic-strain, unit-plastic-strain-rate, room-temperature yield strength, B the strain-hardening constant, n the strain-hardening exponent, C_1 the strain-rate constant, m the thermal-softening exponent and $T_H = (T - T_{room})/(T_{melt} - T_{room})$ a room-temperature (T_{room})-based homologous temperature while T_{melt} is the melting temperature. All temperatures are given in Kelvin. A summary of the Johnson-Cook strength model parameters for AA5083-H131 can be found in Table 1 in Ref 5.

Within the original Johnson-Cook model, Eq 14, temperature provides only a reversible effect in promoting plastic deformation via thermal activation of dislocation glide and climb. Simply stated, higher temperatures promote plastic yielding but, per se, are not considered to (irreversibly) alter material microstructure/properties. However, as pointed out earlier, during FSW, the work-piece material in the weld/stir zone becomes heavily plastically deformed and it becomes generally subjected to temperatures very near, yet lower than, the material melting temperature. Under these conditions, the material tends to undergo annealing at the same time as it is being deformed plastically. In other words, the material in the stir/nugget region tends to dynamically recrystallize, as a result of which the material strength/hardness (at high welding temperatures, as well as, at the room temperature) is lowered relative to that in the base (H131 temper condition) material. This effect of temperature is not accounted for in the original Johnson-Cook model. Rather, only the effect of high temperatures on promoting plastic deformation via thermal activation is taken in to account.

In order to overcome the aforementioned deficiency of the original Johnson-Cook model, a modification is proposed to the differential equation governing the evolution of the equivalent plastic strain. In the original Johnson-Cook model (Ref 43), this evolution was governed by simultaneously satisfying the Hooke's law, yield criterion and flow rule relations (Ref 5). In this way, only the effect of strain-hardening due to an increase in the dislocation density and the resulting increase in the dislocation-motion resistance imposed by the surrounding dislocations is taken into account. In order to include the effects of dynamic recrystallization, a simple phenomenological-based relation for the additional (negative) component in the equivalent plastic strain rate is proposed. This equation is based on the following physics-based arguments:

(a) Dynamic recrystallization is a thermally activated process and consequently the correction term in the equivalent plastic strain evolution equation must contain a Boltzmann probability term in the form $\exp(-Q/RT)$, where Q is the activation energy while R is the universal gas-constant. In other words, the dynamic-recrystallization correction to the Johnson-Cook strength model should be an Arrhenius-type function;
(b) Since the rate of recrystallization across various alloy systems appear to scale with the dimensionless absolute-zero based homologous temperature, T_h, (defined as the ratio of the temperature and the melting temperature, both temperatures expressed in K), it is convenient to replace Q/RT term in the Boltzmann probability relation with q/T_h, where q is a dimensionless activation energy; and
(c) Owing to the fact that the rate at which material tends to recrystallize increases as the amount of cold work is increased, q should be a decreasing function of the equivalent plastic strain $\bar{\varepsilon}_{pl}$.

Based on these arguments, the dynamic-recrystallization contribution to the evolution of the equivalent plastic strain, can be expressed as

$$\dot{\bar{\varepsilon}}_{pl,dyn\_rec} = \dot{\bar{\varepsilon}}_{0,pl,dyn\_rec} e^{\left(-q\left(\bar{\varepsilon}_{pl}\right)/T_h\right)} \quad \text{(Eq 15)}$$

where $\dot{\bar{\varepsilon}}_{0,pl,dyn\_rec}$ is a dynamic-recrystallization frequency/pre-exponential term. An analysis of the available experimental data pertaining to the kinetics of recrystallization of AA5083 (Ref 44) showed that q scales inversely with $\bar{\varepsilon}_{pl}$ raised to a power of 2.9. Based on this finding and using the curve-fitting results for the experimental recrystallization-kinetics data reported in Ref 44, it is found that Eq 15 can be rewritten as

$$\dot{\bar{\varepsilon}}_{pl,dyn\_rec} = 21.5 e^{-1/\left(\bar{\varepsilon}_{pl}^{2.9} T_h\right)} \quad \text{(Eq 16)}$$

The effect of Eq 16 on modifying the behavior of AA5083 under simple uniaxial tensile conditions is displayed in Fig. 3(a)-(c). In Fig. 3(a), it is seen that when T_h is relatively low ($T_h = 0.3$), the effects of dynamic recrystallization are small so that the material strain hardens. In sharp contrast, when T_h is relatively high ($T_h = 0.9$), the effect of dynamic recrystallization is dominant so that despite extensive plastic deformation, the material undergoes pronounced strain softening, Fig. 3(b). In Fig. 3(c), it is seen that when the effects of strain hardening and dynamic recrystallization are comparable, at the intermediate values of T_h ($T_h = 0.5$), no significant change in material strength takes place during plastic deformation. The oscillating behavior of material strength seen in Fig. 3(c) is a result of the competition and the interaction between strain-hardening and dynamic recrystallization-induced softening processes. That is, softer material tends to harden at a high rate and, when the amount of plastic strain in the work-piece becomes sufficiently large, the rate of dynamic recrystallization becomes high enough to bring the strength down. This type of oscillating-strength behavior is often a signature of the undergoing dynamic-recrystallization process.

It should be recognized that the kinetics of recrystallization is generally described using the so-called Johnson-Mehl-Avrami equation (e.g., Ref 45-47). Within this equation, the volume fraction of the material recrystallized, as a function of time, is given by a characteristic S-shaped curve which starts from a non-zero annealing time (the incubation period), increases with a higher and higher slope and, ultimately, the slope decreases as the volume fraction of the recrystallized material approaches unity, Fig. 4. The inner steepest part of this curve generally covers the major portion (80-90%) of the range of the recrystallized-material volume-fraction. Taking this fact into account, the simple model proposed here assumes that the entire recrystallized-material volume-fraction versus time curve can be represented by its inner part, and that this portion can be linearized. The slope of this new linear function, on the other hand, is taken to be a function of the temperature and the

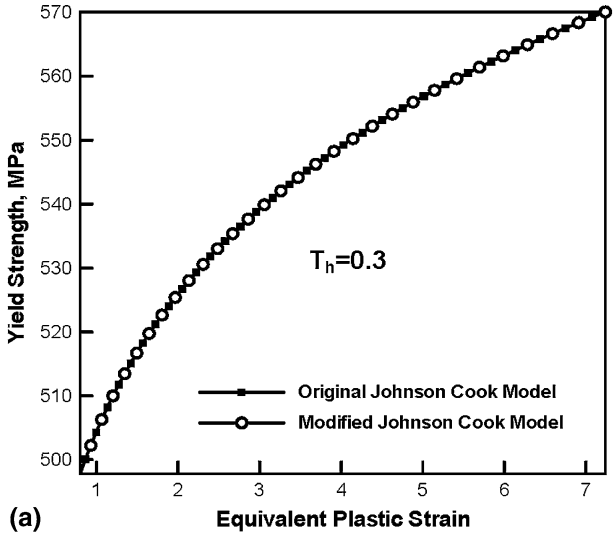

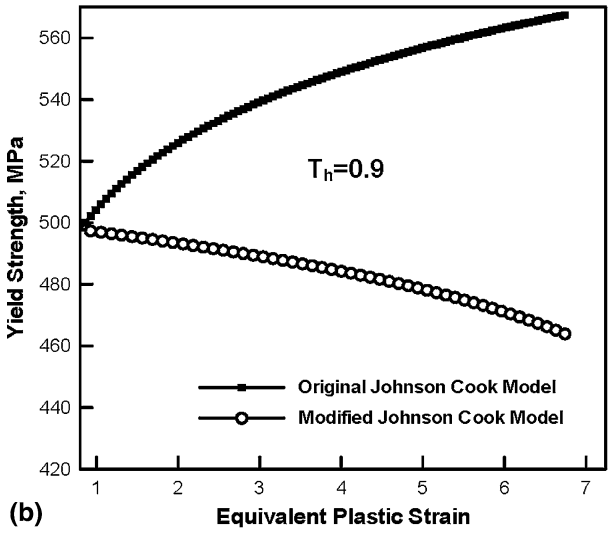

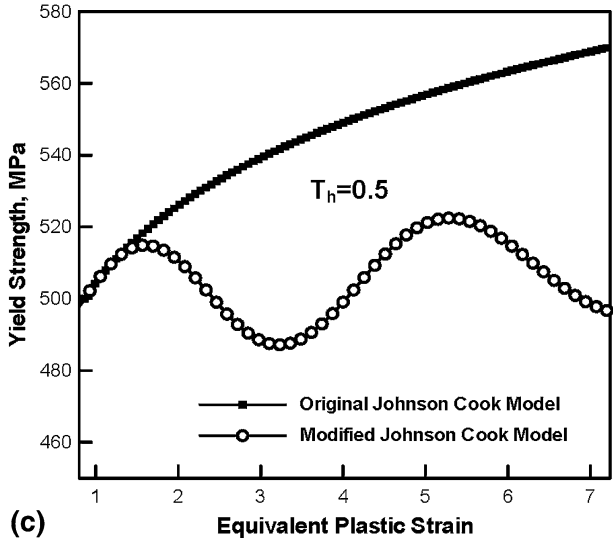

Fig. 3 A comparison of the strength vs. equivalent plastic strain curves as predicted by the original and the modified Johnson-Cook strength models. The results are obtained under uniaxial strain-rate of 0.001 s^{-1} and at three different homologous temperatures: (a) θ = 0.3; (b) θ = 0.9; (c) θ = 0.5

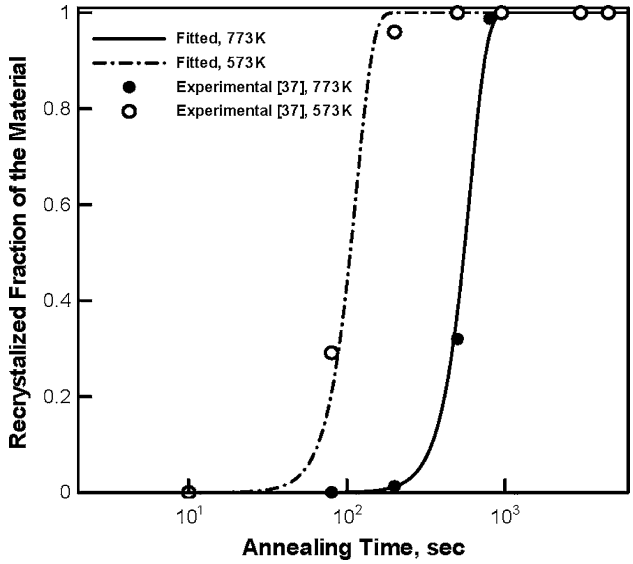

Fig. 4 Experimental results (Ref 44) and the fitting curves pertaining to the recrystallization kinetics in AA5083

equivalent plastic strain. Equation 16 is then obtained by assuming that $\dot{\bar{\varepsilon}}_{pl,dyn\_rec}$ scales linearly with the rate of recrystallization.

In order to include the effects of dynamic recrystallization of the work-piece material on the material evolution during FSW, the modified Johnson-Cook material model is implemented into a user-material subroutine *VUMAT.for* and linked with ABAQUS/Explicit finite-element solver. In order to validate the implementation of the material model, several FSW cases were analyzed. It is found that when the effects of dynamic recrystallization are suppressed, the results (not shown for brevity), based on the user-material model and the Johnson-Cook model (built in the ABAQUS/Explicit) are essentially identical.

4.2 Representative Computational Results

In this section, examples of the typical results obtained in the fully coupled finite element investigation of the FSW process carried out in this study are presented and discussed. The finite element analysis used allowed investigation of the effect of all the key FSW process parameters on the temporal evolution and spatial distribution of various material-related quantities, such as temperature, stress, and strain components, equivalent plastic strain, local material strength, material velocity, trajectory of tracer particles which reveal locations of the associated material particles as they are passing through the circular region surrounding the rotating pin tool, etc. For brevity, only few representative and unique results will be displayed and discussed in this section.

4.2.1 Equivalent Plastic Strain Field. An example of the typical results pertaining to spatial distribution and temporal evolution of the equivalent plastic strain in the work-piece during FSW is displayed in Fig. 5(a)-(d). Simple examination of the results displayed in these figures and of the results obtained in this study(but not shown for brevity) reveals that:

(a) Depending on the FSW process conditions such as tool contact pressure, tool rotational, and translational speeds,

equivalent plastic strains in a range between 20 and 50 are observed;

(b) The highest equivalent plastic strains are always found in the work-piece material right below the tool shoulder, and equivalent plastic strains progressively decreased from this region as a function of the distance in the radial and through-the-thickness directions;

(c) There is a highly pronounced asymmetry in the distribution of the equivalent plastic strain relative to the initial location of the butting surfaces. This asymmetry is related to the aforementioned differences in the material transport (at the advancing and the retreating sides of the weld) from the region ahead of the tool to the region behind the tool; and

(d) As the tool Translational speed is decreased and the tool/work-piece contact pressure is increased, higher equivalent plastic strains are observed and equivalent plastic strain differences between the top and bottom surfaces of the work-piece are reduced. This finding suggests that under these FSW process conditions, the extent of material stirring/mixing (which plays a critical role in weld quality/joint-strength) is increased.

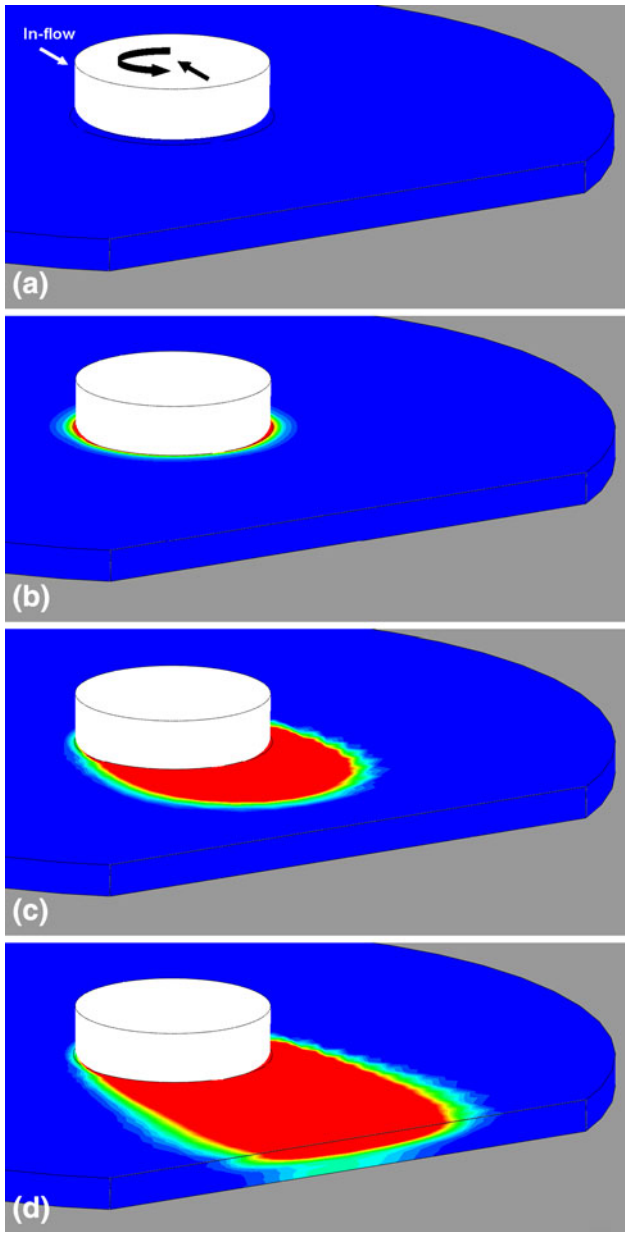

Fig. 5 Typical results pertaining to spatial distribution and temporal evolution of the equivalent plastic strain during FSW: (a) zero-time step; (b) at the end of tool-insertion; (c) 7 s afterwards; and (d) 14 s afterwards. Equivalent-plastic strain range: 0.0 (dark gray) to 50.0 (lighter gray in contact with the tool)

4.2.2 Material/Tracer Particle Trajectories. An example of the typical results pertaining to temporal evolution of the position of two material particles (located initially in the through-the-thickness mid-plane of the work-piece) is displayed in Fig. 6(a)-(d). It should be noted that due to the ALE character of the finite-element analysis used in this study, the motion of the finite-element mesh is not completely tied to the motion of the material. In fact, as seen in Fig. 6(a)-(d), the mesh is continuously re-meshed and, hence, remains similar to the initial mesh, while material particles continues to move. In order to observe the motion of material particles during FSW, the so-called tracer particles option was used within ABAQUS/Explicit. Simple examination of the results displayed in Fig. 6(a)-(d) and of the results obtained in this study (but not shown for brevity) reveals the following basic aspects of the FSW process:

(a) The material at the advancing side either simply passes over to the retreating side and then simply passes through the weld-nugget zone (as represented by the red tracer-particle) or, on entering the stir/nugget zone, makes few cycles around the tool-pin and is co-stirred with some of the retreating-side material to form the welded joint (as represented by the yellow tracer-particle);

(b) The work-piece material at the retreating side does not, for the most part, enter the stir zone under the tool-shoulder and usually only flows around it; and

(c) The advancing-side material further away from the initial butting surfaces remains on the advancing side and either enters the stir region on the advancing side or flows around it.

4.2.3 Temperature Field. An example of the typical results pertaining to spatial distribution of the work-piece temperature in the work-piece during FSW is displayed in Fig. 7(a)-(d). The results displayed in Fig. 7(a) and (b) refer to the temperature distributions over the medial longitudinal and medial transverse sections, respectively. Simple examination of the results displayed in these figures and of the results obtained in this study (but not shown for brevity) reveals that:

(a) Depending on the FSW process conditions such as tool contact pressure, tool rotational and travel speeds, temperatures in a range between 350 and 450 °C are obtained;

(b) The highest temperatures are always found in the work-piece material right below the tool shoulder, and temperatures progressively decrease from this region as a function of the distance in the radial and through-the-thickness directions;

(c) Temperature distribution in the transverse direction is clearly asymmetric and, in the longitudinal direction, larger thermal gradients are observed in the regions in front of the tool;

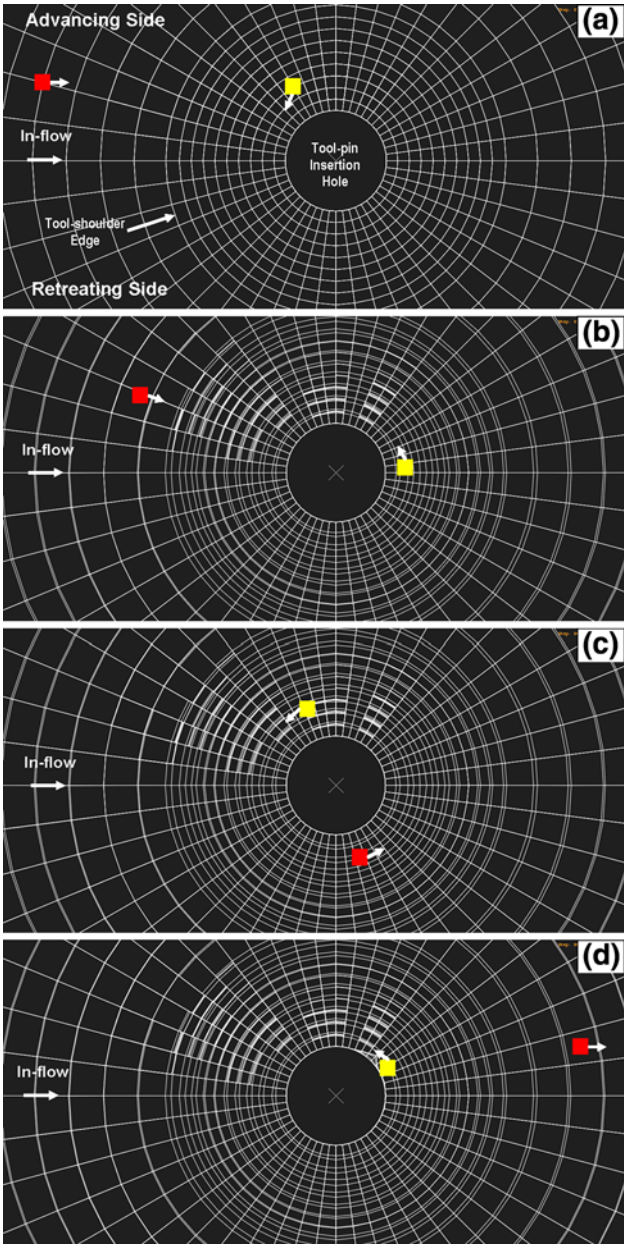

Fig. 6 Spatial location of two advancing-side material particles at four consecutive 5-s intervals

(d) As the tool rotational speed and contact pressure are increased, higher temperatures are observed, and temperature differences between the top and bottom surfaces of the work piece are reduced; and
(e) Typically plastic deformation contributes around 30% to the overall heat generation (the remainder is associated with the frictional dissipation at the tool/work piece contact surfaces) and the plastic-strain contribution increases slowly with an increase in the translational velocity of the tool.

4.2.4 Residual Stress Field. As discussed earlier, friction stir-welded components may contain significant levels of the residual stresses both in the direction of welding (the longitudinal direction) and in the direction normal to it (the transverse direction). These residual stresses are caused by non-uniform distributions in the extent of plastic deformations (as represented by the equivalent plastic strains) and in temperature in different regions within the weld joint. Since the presence of residual stresses can significantly affect the structural and environmental resistance/durability of welded joints, it is critical that they are quantified and that their magnitudes and spatial distributions be correlated with various FSW process parameters. While a comprehensive investigation of the residual stress distribution as a function of the FSW process parameters is beyond the scope of this study, an effort was invested here to develop computational capabilities for such investigations. With this objective, the results of the FSW simulation are imported into the implicit finite-element program ABAQUS/Standard, and a quasi-static fully coupled thermo-mechanical analysis is carried out. It should be noted that ABAQUS/Explicit is not suitable for this type of investigation since it requires prohibitively long computational times. Within the quasi-static fully coupled thermo-mechanical analysis employed, the FSW tool is removed and the boundary conditions are eliminated from the work-piece while temperature is progressively decreased down to room temperature.

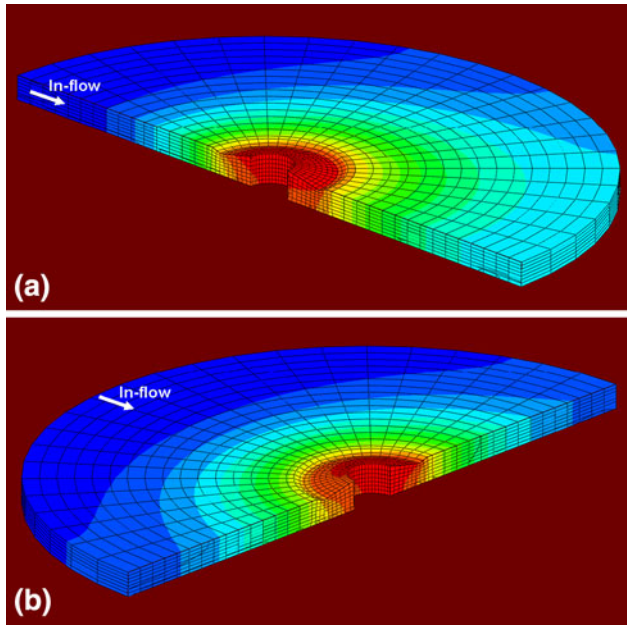

Fig. 7 Typical temperature distribution over one-half of the work-piece obtained by cutting along: (a) the longitudinal; and (b) transverse directions: maximum (lighter gray surrounding the tool insertion hole) = 400 °C; minimum (dark gray) = 25 °C

An example, of the results pertaining to the distribution of longitudinal and transverse residual stresses over a transverse sections of the work-piece, is displayed in Fig. 8(a) and (b), respectively. Simple examination of the results displayed in these figures and of the results obtained in this study (but not shown for brevity) reveals that:

(a) Maximum longitudinal residual stresses are generally higher then their maximum transverse counterparts by a factor of roughly two;
(b) The residual stresses typically increase in magnitude as the distance from the initial portion of butting surfaces is reduced. However, in the innermost portion of the

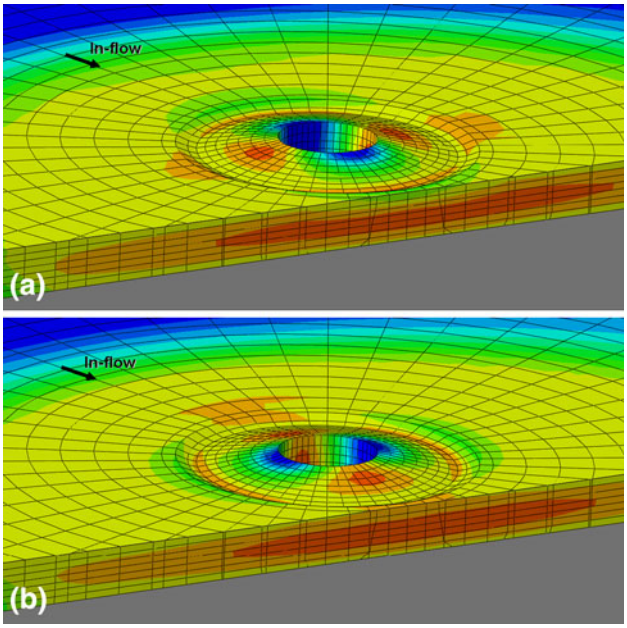

Fig. 8 Typical: (a) longitudinal, and (b) transverse residual-stress distributions over the transversely sectioned work-piece. Longitudinal-stress range; minimum (dark gray) = −21 MPa and maximum (lighter gray surrounding the tool insertion hole) = 72 MPa. Transverse-stress range; minimum (dark gray) = −12 MPa and maximum (lighter gray surrounding the tool insertion hole) = 39 MPa

nugget, they tend to decrease somewhat. This is clearly related to the effect of dynamic recrystallization which is prevalent in this region; and

(c) Both the longitudinal and transverse residual stresses tend to increase with an increase in the tool rotational and travel velocities.

4.3 Validation of the Present Computational Approach

The results presented in the previous section (as well as the results obtained in this study but not shown) appear to be quite reasonable and in good qualitative agreement with their experimental counterparts overviewed in Sect 2. However, if the computational approach similar to the one developed here is to become an integral part of the FSW practice and help guide further development and optimization of this metal-joining process, then it must also demonstrate the needed level of quantitative agreement with the experimental results/findings. In order to assess the ability of the present computational approach to account for the experimentally measured FSW-related results, selected computational results are compared with their experimental counterparts obtained in the study of Peel et al. (Ref 40). The study carried out in Ref 40 is quite comprehensive and thorough and involves AA5083, the aluminum alloy investigated in this study. While the study of Peel et al. (Ref 40) yielded numerous results, only the following two sets of these results could be directly compared with the finite-element based computational results obtained in this study: (a) variation of the longitudinal and transverse (normal) residual stresses as a function of the distance from the weld line; and (b) variation of the room-temperature material strength as a function of the distance from the weld line.

4.3.1 Residual Stress Distribution. A comparison between the computed results of this study and the experimentally measured results reported in Ref 40 pertaining to variation of the longitudinal and transverse residual stresses as a function of the distance from the initial location of the butting surfaces is displayed in Fig. 9(a) and (b). Two sets of computational results are presented: one based on the use of the original Johnson-Cook material model and the other based on the use of the solidified Johnson-Cook model. Simple examination of the results presented in Fig. 9(a) and (b) shows that the results based on the modified Johnson-Cook model are in better agreement with the experimental results. While some disagreement exists between the computational results based on the modified Johnson-Cook model and the experimental results, the overall residual stress distribution profile appears to be reasonably well reproduced by the present computational analysis. Specifically:

(a) The residual stresses are compressive at larger distances from the weld-line at the advancing side of the weld (the right-hand side in Fig. 9a and b);
(b) As one approaches the weld-line at the advancing side, the residual stresses first increase in magnitude and then switch their character (i.e., becomes tensile), at a distance of 15-20 mm from the weld-line (at the advancing side);
(c) In the innermost portion of the nugget, the tensile residual stresses tend to decrease somewhat;
(d) As the distance from the weld-line increases on the retreating side, the stresses gradually decrease toward zero; and
(e) The longitudinal residual stresses are generally higher than their transverse counterparts.

4.3.2 Room-Temperature Material Strength Distribution. A comparison between the computed results of this study (as predicted by the original and modified Johnson-Cook strength models) and the experimentally measured results reported in Ref 40 pertaining to variation of the room-temperature material strength as a function of the distance from the initial location of the butting surfaces is displayed in Fig. 10. The results displayed in this figure show that, while the quantitative agreement between the computed results based on the modified Johnson-Cook model and the experimental results is only fair, the computational analysis of this study correctly predicts the overall trend. This is quite encouraging considering the fact that the results based on the original Johnson-Cook strength model (in which the effect of dynamic recrystallization is neglected) incorrectly predict that the highest room-temperature strength levels are located in the innermost region of the nugget zone (where the equivalent plastic strain levels are also the highest).

5. Conclusions

Based on the results and above discussions of this study, the following main summary remarks and conclusions can be made:

1. A brief overview of the processing/property/performance relations and the fundamentals of heat and mass flow accompanying friction stir welding (FSW) is conducted.

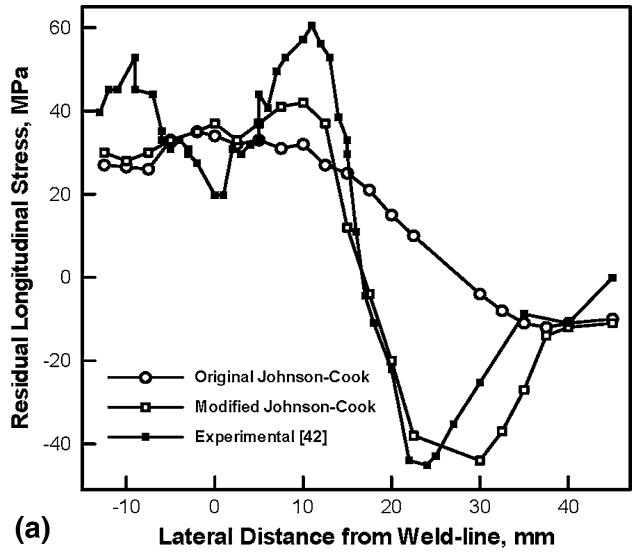

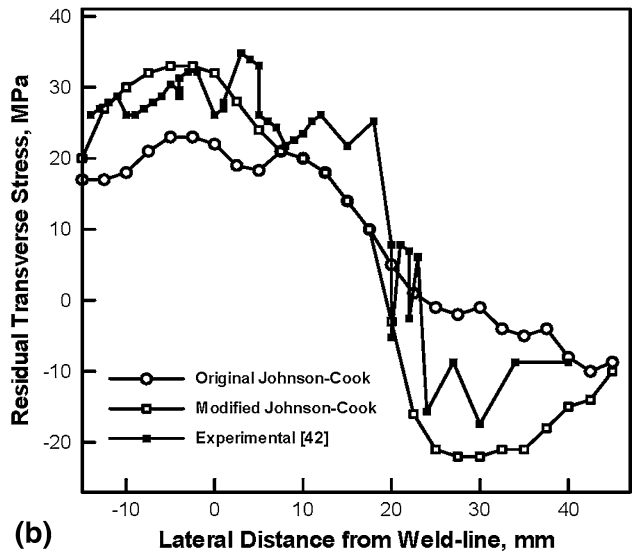

Fig. 9 Variation of the (a) longitudinal and (b) transverse residual stresses as a function of the distance from the weld-line. Data pertaining to the advancing side of the weld joint are on the right-hand side of the plot

2. A fully coupled thermo-mechanical finite-element analysis of the FSW process and the FSW-behavior of a solution-strengthened and strain-hardened aluminum alloy is carried out.
3. It was shown that the present computational procedure can account, qualitatively, quite well for most of the experimental observations pertaining to the effect of various FSW process parameters on the heat/material flow and the FSW-joint formation.
4. The results obtained further show that reasonable good quantitative agreement between the model predictions and the experimental results pertaining to the spatial distribution of post-welding residual-stress and material-strength can be attained only if proper modifications in the work-piece material strength model are made to include the effect of dynamic recrystallization.

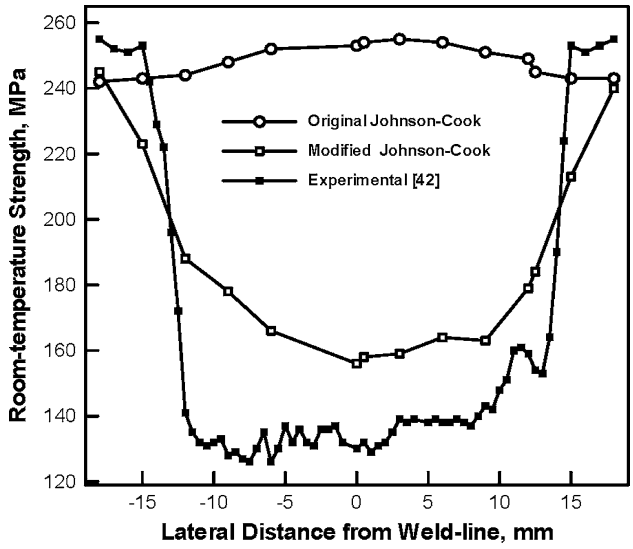

Fig. 10 Variation of the room-temperature material strength as a function of the distance from the weld-line. Data pertaining to the advancing side of the weld joint are on the right-hand side of the plot

Acknowledgments

This research article is based on project with financial support under the U.S. Army/Clemson University Cooperative Agreements, W911NF-04-2-0024 and W911NF-06-2-0042.

References

1. W.M. Thomas, E.D. Nicholas, J.C. Needham, M.G. Murch, P. Temple-Smith, and C.J. Dawes. Friction Stir Butt Welding, International Patent Application No. PCT/GB92/02203, 1991
2. C.J. Dawes and W.M. Thomas, Friction Stir Process Welds Aluminum Alloys, *Weld. J.*, 1996, **75**, p 41–52
3. W.M. Thomas and R.E. Dolby, Friction Stir Welding Developments, *Proceedings of the Sixth International Trends in Welding Research*, S.A. David, T. DebRoy, J.C. Lippold, H.B. Smartt, and J.M. Vitek, Ed. (Materials Park, OH, USA), ASM International, 2003, p 203–211
4. R. Nandan, T. DebRoy, and H.K.D.H. Bhadeshia, Recent Advances in Friction-Stir Welding—Process, Weldment Structure and Properties, *Prog. Mater. Sci.*, 2008, **53**, p 980–1023
5. M. Grujicic, T. He, G. Arakere, H.V. Yalavarthy, C.-F. Yen, and B.A. Cheeseman, Fully-Coupled Thermo-Mechanical Finite-Element Investigation of Material Evolution During Friction-Stir Welding of Aa5083, *J. Eng. Manuf.*, Sept 2009 (accepted for publication)
6. M.B. Bever, D.L. Holt, and A.L. Titchener, Stored Energy of Cold Work, *Prog. Mater. Sci.*, 1973, **17**, p 5–192
7. Q. Zhu, C.M. Sellars, and H.K.D.H. Bhadeshia, Quantitative Metallography of Deformed Grains, *Mater. Sci. Technol.*, 2007, **23**(7), p 757–766
8. M.V. Belous and V.T. Cherepin, Changes in the Steel Carbide Phase Under Influence of Cold Plastic Deformation, *Fiz. Met. Metalloved*, 1962, **14**, p 48–54
9. F. Danoix, D. Julien, X. Sauvage, and J. Copreaux, Direct Evidence of Cementite Dissolution in Drawn Pearlitic Steels Observed by Tomographic Atom Probe, *Mater. Sci. Eng. A*, 1998, **250**, p 8–13
10. M. Umemoto, Z.G. Liu, X.J. Hao, K. Masuyama, and K. Tsuchiya, Formation of Nanocrystalline Ferrite Through Rolling and Ball Milling, *Mater. Sci. Forum*, 2001, **12**, p 167–174
11. Y. Ivanisenko, I. MacLaren, R.Z. Valiev, and H.J. Fecht, First Observation of a Shear-Induced Bcc to Fcc Transformation in Nanocrystalline Ferrite, *Adv. Eng. Mater.*, 2005, **7**, p 1011–1014

12. W. Lojkowski, Yu. Ivanisenko, and H.-J. Fecht, Strain Induced Cementite Dissolution in Pearlitic Steels as a Classical Example of Mechanical Alloying, *Trans. Indian Inst. Met.*, 2005, **13**, p 939–1227
13. E.S. Gorkunov, S.V. Grachev, S.V. Smirnov, V.M. Somova, S.M. Zadvorkin, and L.E. Kar'kina, Relation of Physical-Mechanical Properties to the Structural Condition of Severely Deformed Patented Carbon Steels at Drawing, *Russ. J. Nondestruct. Test.*, 2005, **41**, p 65–79
14. M.J. Russell and H. Shercliff, Analytical Modelling of Friction Stir Welding, *INALCO'98: Seventh International Conference on Joints in Aluminium*, M.J. Russell and R. Shercliff R, Ed. (Cambridge, UK) TWI, 1999, p 197–207
15. M.Z.H. Khandkar, J.A. Khan, and A.P. Reynolds, Prediction of Temperature Distribution and Thermal History During Friction Stir Welding: Input Torque Based Model, *Sci. Technol. Weld. Join.*, 2003, **10**, p 165–174
16. S. Xu, X. Deng, A.P. Reynolds, and T.U. Seidel, Finite Element Simulation of Material Flow in Friction Stir Welding, *Sci. Technol. Weld. Join.*, 2001, **6**, p 191–193
17. K.V. Jata and S.L. Semiatin, Continuous Dynamic Recrystallization During Friction Stir Welding, *Scripta Mater.*, 2000, **12**, p 743–748
18. R. Nandan, G.G. Roy, and T. DebRoy, Numerical Simulation of Three-Dimensional Heat Transfer and Plastic Flow During Friction Stir Welding, *Metall. Mater. Trans. A*, 2006, **37**, p 1247–1259
19. R. Nandan, G.G. Roy, and T. DebRoy, Three-Dimensional Heat and Material Flow During Friction Stir Welding of Mild Steel, *Acta Mater.*, 2007, **12**, p 883–895
20. R. Nandan, T.J. Lienert, and T. DebRoy, Toward Reliable Calculations of Heat and Plastic Flow During Friction Stir Welding of Ti-6Al-4V Alloy, *Int. J. Mater. Res.*, 2008, **9**, p 434–444
21. P.J. Withers and H.K.D.H. Bhadeshia, Residual Stress. Part II: Nature and Origins, *Mater. Sci. Technol.*, 2001, **17**, p 366–375
22. J.A. Francis, H.J. Stone, S. Kundu, R.B. Rogge, H.K.D.H. Bhadeshia, and P.J. Withers, Transformation Temperatures and Welding Residual Stresses in Ferritic Steels, *Proceedings of PVP2007, ASME Pressure Vessels and Piping Division Conference* (San Antonio, Texas), American Society of Mechanical Engineers (ASME), 2007, p 1–8
23. H.N.B. Schmidt, T.L. Dickerson, and J.H. Hattel, Material Flow in Butt Friction Stir Welds in AA2024-T3, *Acta Mater.*, 2006, **54**(4), p 1199–1209
24. L. Fratini, G. Buffa, D. Palmeri, J. Hua, and R. Shivpuri, Material Flow in FSW of AA7075-T6 Butt Joints: Numerical Simulations and Experimental Verifications, *Sci. Technol. Weld. Join.*, 2006, **11**(4), p 412–421
25. M.Z.H. Khandkar, J.A. Khan, and A.P. Reynolds, Prediction of Temperature Distribution and Thermal History During Friction Stir Welding: Input Torque Based Model, *Sci. Technol. Weld. Join.*, 2003, **8**, p 165–174
26. K.V. Jata and S.L. Semiatin, Continuous Dynamic Recrystallization During Friction Stir Welding, *Scripta Mater.*, 2000, **12**, p 743–748
27. R. Nandan, T.J. Lienert, and T. DebRoy, Toward Reliable Calculations of Heat and Plastic Flow During Friction Stir Welding of Ti-6Al-4V Alloy, *Int. J. Mater. Res.*, 2008, **99**, p 434–444
28. Y. Sato, M. Urata, and H. Kokawa, Parameters Controlling Microstructure and Hardness During Friction-Stir Welding of Precipitation-Hardenable Aluminum Alloy 6063, *Metall. Mater. Trans. A*, 2002, **33**(3), p 625–635
29. M.J. Peel, A. Steuwer, P.J. Withers, T. Dickerson, Q. Shi, and H. Shercliff, Dissimilar Friction Stir Welds in AA5083-AA6082. Part I: Process Parameter Effects on Thermal History and Weld Properties, *Metall. Mater. Trans. A*, 2006, **37**(7), p 2183–2193
30. W.M. Thomas, K.I. Johnson, and C.S. Wiesner, Friction Stir Welding-Recent Developments in Tool and Process Technologies, *Adv. Eng. Mater.*, 2003, **5**, p 485–490
31. W.M. Thomas, Friction Stir Welding—Recent Developments, *Mater. Sci. Forum*, 2003, **426–432**, p 229–236
32. W.M. Thomas, D.G. Staines, K.I. Johnsonand, and P. Evans, ComStir—Compound Motion for Friction Stir Welding and Machining, *Adv. Eng. Mater.*, 2003, **5**, p 273–274
33. Y.H. Zhao, S.B. Lin, F. Qu, and L. Wu, Influence of Pin Geometry on Material Flow in Friction Stir Welding Process, *Mater. Sci. Technol.*, 2006, **22**, p 45–50
34. R. Crawford, G.E. Cook, A.M. Strauss, D.A. Hartman, and M.A. Stremler, Experimental Defect Analysis and Force Prediction Simulation of High Weld Pitch Friction Stir Welding, *Sci. Technol. Weld. Join.*, 2006, **11**, p 657–665
35. H.J. Liu, H. Fujii, M. Maeda, and K. Nogi, Tensile Fracture Location Characterisation of Friction Stir Welded Joints of Different Aluminium Alloys, *J. Mater. Sci. Technol.*, 2004, **20**, p 103–105
36. X. Long and S.K. Khanna, Modelling of Electrically Enhanced Friction Stir Welding Process Using Finite Element Method, *Sci. Technol. Weld. Join.*, 2005, **10**, p 482–487
37. Y.G. Kimand, H. Fujii, T. Tsumura, T. Komazaki, and K. Nakata, Three Defect Types in Friction Stir Welding of Aluminium Die Casting Alloys, *Mater. Sci. Eng. A*, 2006, **415**, p 250–254
38. K. Elangovan and V. Balasubramanian, Influences of Pin Profile and Rotational Speed of the Tool on the Formation of Friction Stir Processing Zone in AA2219 Aluminium Alloy, *Mater. Sci. Eng. A*, 2007, **459**, p 7–18
39. P.J. Withers and H.K.D.H. Bhadeshia, Residual Stress. Part 1: Measurement Techniques, *Mater. Sci. Technol.*, 2001, **17**, p 355–365
40. M. Peel, A. Steuwer, M. Preuss, and P.J. Withers, Microstructure, Mechanical Properties and Residual Stresses as a Function of Welding Speed in Aluminium AA5083 Friction Stir Welds, *Acta Mater.*, 2003, **51**(16), p 4791–4801
41. M.Z.H. Khandkar, J.A. Khan, A.P. Reynolds, and M.A. Sutton, Predicting Residual Thermal Stresses in Friction Stir Welded Metals, *J. Mater. Process. Technol.*, 2006, **174**, p 195–203
42. ABAQUS Version 6.8-1, User Documentation, Dassault Systems, 2008, p 1–254
43. G.R. Johnson and W.H. Cook, A Constitutive Model and Data for Metals Subjected to Large Strains, High Strain Rates and High Temperatures, *Proceedings of the 7th International Symposium on Ballistics*, 1983
44. K. Kannan, J.S. Vetrano, and C.H. Hamilton, Effects of Alloy Modification and Thermomechanical Processing on Recrystallization of Al-Mg-Mn Alloys, *Metall. Mater. Trans. A*, 1996, **27**(10), p 2947–2957
45. R.E. Reed-Hill, *Physical Metallurgy Principles*, PWS Publishing Company, Massachusetts, 1994
46. D.C. Hofmann and K.S. Vecchio, Thermal History Analysis of Friction Stir Processed and Submerged Friction Stir Processed Aluminum, *Mater. Sci. Eng. A*, 2007, **465**(1–2), p 165–175
47. W. Woo, Z. Feng, X.L. Wang, D.W. Brown, B. Clausen, and K. An, In Situ Neutron Diffraction Measurements of Temperature and Stresses During Friction Stir Welding of 6061-T6 Aluminium Alloy, *Sci. Technol. Weld. Join*., 2007, **12**(4), p 298–303